# Preprints.org

Article

# Monitoring Distribution of the Therapeutic Agent Dimethyl sulfoxide (DMSO) via Solvatochromic Shift of the Albumin-Bound Indocyanine Green

Jaedu Cho , Farouk Nouizi , Chang-Seok Kim , Gultekin Gulsen [*]

*Article*

# Monitoring Distribution of the Therapeutic Agent Dimethyl sulfoxide (DMSO) via Solvatochromic Shift of the Albumin-Bound Indocyanine Green

**Jaedu Cho** [1,2]**, Farouk Nouizi** [1]**, Chang-Seok Kim** [2] **and Gultekin Gulsen** [1,]*

[1] Tu and Yuen Center for Functional Onco-Imaging, Departments of Radiological Sciences, University of California Irvine, CA 92697, USA

[2] Department of Cogno-Mechatronics Engineering, Pusan National University, Busan 607-735, Korea

\* Correspondence: ggulsen@uci.edu

**Abstract:** We recently developed a novel hyperspectral excitation-resolved near-infrared fluorescence imaging system (HER-NIRF) based on a continuous-wave wavelength-swept laser. In this study, this technique is applied for measuring the distribution of the therapeutic agent dimethyl sulfoxide (DMSO) by utilizing solvatochromic shift in the spectral profile of albumin-bound Indocyanine green (ICG). Using wide-field imaging in turbid media, complex dynamics of albumin-bound ICG is measured in mixtures of dimethyl sulfoxide (DMSO) and water. Phantom experiments are conducted to evaluate the performance of the HER-NIRF system. The results show that the distribution of DMSO can be visualized in the wide-field reflection geometry. One of the main purposes of the DMSO is to act as a carrier for other drugs, enhancing their effects by facilitating skin penetration. Understanding solubility and permeability of drugs in vivo is very important in drug discovery and development. Hence, this HER-NIRF technique has a great potential to advance the utilization of the therapeutic agent DMSO by mapping its distribution via solvatochromic shift of ICG. By customizing the operational wavelength range, this system can be applied to any other fluorophores in the near infrared region and utilized for a wide variety of drug delivery studies.

**Keywords:** fluorescence imaging; multispectral and hyperspectral imaging; solvatochromic shift tunable lasers; spectroscopy; dmso sensing; drug uptake monitoring

## 1. Introduction

Dimethyl sulfoxide (DMSO) is one of the most commonly used pharmaceutical drugs in life sciences. It has a wide spectrum of pharmacological effects, including anti-inflammatory effects, local analgesia, weak bacteriostasis and most importantly membrane penetration. DMSO is not only used on animals and humans itself by various routes including dermal and oral, but also utilized to enhance absorption of many other chemicals along these same routes. At low concentrations, DMSO exhibits anti-inflammatory, analgesic, diuretic, vasodilator, anti-platelet aggregation, radio-protective, and muscle-relaxing properties [1]. The observed beneficial effects on skin rejuvenation and recovery from thermal injury might be explained by its effective property of being a vigorous scavenger of hydroxyl free radical. Accordingly, it has been applied for a variety of purposes, such as treatment of musculoskeletal and dermatological diseases, cryopreservation of stem cells, treatment of interstitial cystitis, treatment of increased intracranial pressure, and many more [2–7].

One of the principal uses of the DMSO is as a vehicle for other drugs, thereby enhancing the effect of the drug, and aiding penetration of other drugs into the skin. For example, it is now well established as a penetration enhancer in topical pharmaceutical formulations. The permeability of drugs to the skin essentially requires that the retained epidermis should be diffused by the drug. DMSO is a safe and effective mechanism for facilitating the transdermal delivery of both hydrophilic and lipophilic medications to provide localized drug delivery.[8] The effect on cell membranes depends on the concentration of DMSO, from an increased bilayer-fluidity at lower concentrations, through to the formation of water pores and the extraction of lipid molecules at higher

concentrations.[9] Therefore, capability of measuring the local concentration of the DMSO in vivo is important. In addition to these, DMSO is also utilized in other delivery strategies to overcome issues of solubility such as particle size reduction by micronizing the active compound or the use of nanocarriers as a vehicle. As one of those methods, the supercritical antisolvent (SAS) technique utilizes DSMO regularly[10]. Another example of such a technique is SALT, solvent-assisted active loading technology, which was developed to promote active loading of poorly soluble drugs in the liposomal core to improve the encapsulation efficiency and formulation stability. [11]

Depending on the application type and its dose, DMSO can induce adverse effects including generation of oxidative stress and cytotoxicity [12]. When used for the preservation of liquid nitrogen-frozen stem cells, for example, DMSO associated with toxicity in the transplant recipient in a prospective noninterventional study in 64 European Blood and Marrow Transplant Group centers undertaking autologous transplantation on patients with myeloma and lymphoma.[13] Meanwhile, Madsen et al. reviewed a total of 109 different clinical studies involving intravenous, transdermal, oral, and intravenous administration of DSMO. They showed that gastrointestinal and skin reactions were the commonest reported adverse reactions [14]. Most importantly, their investigation confirmed a relationship between the given dose of DMSO and the occurrence of adverse reactions.

Since the dose plays an important role in the occurrence of adverse reactions, it is important to have a technique that can provide the distribution and dose of the DSMO. Moreover, DSMO dose also play a critical role effect on cell membranes and hence, the delivery of the drugs. The solubility of the DMSO-mixed water-insoluble drugs depends on the local residual level of the DMSO, and permeability of the drugs decreases by precipitation of the drugs in biological media. Therefore, a technique that can monitor the DSMO concentration will play a critical role in the investigation of the optimum dose of the DMSO for a particular application, from increasing the efficiency of drug delivery to reduce the adverse reactions. Such a technique may also guide the applied DMSO dose real time during these therapeutic applications.

Saar et al. have demonstrated molecular imaging visualizing DMSO with a stimulated Raman scattering technique [3]. However, this nonlinear microscopy is inadequate for wide-field imaging with an organ-level field of view. Meanwhile, it has long been known that UV/vis/near-IR absorption spectra of chemical compounds may be influenced by the surrounding medium and that solvents can bring about a change in the position, intensity, and shape of absorption bands [15]. Measuring the environment polarity in different media has been studied extensively with optical fluorescent dyes using solvatochromism [4]. Indeed, optical dyes are used for this purpose since their molecular spectral profiles are significantly affected by the local polarity of biological media. These compounds whose absorption and emission spectra depend on the environment polarity are known as solvatochromic dyes, which can operate in a wide range of the optical spectrum including ultraviolet, visible, and near-infrared (NIR, ~650-950 nm). However, it is challenging to perform solvatochromic dye-mediated polarity measurements in vivo since these dyes unfortunately have heavily overlapping excitation and emission spectra and exhibit weak solvatochromic shifts in their spectral profiles. Moreover, tissue optical properties affect the measured fluorescence spectra [5,6].

Establishing a regular solvatochromic response to various DSMO concentration can serve as a technique for DMSO sensing. Truksa et al. very recently investigated the change in absorption and emission spectra of lumazine, alloxazine and their cyanated or fluorinated derivatives with DSMO [16]. They measured the modulated spectroscopic properties by varying water concentration in DMSO solutions. Cyano-substituted lumazine has shown a remarkable sensitivity for the relative DMSO-water concentrations, including an unexpected behavior in the solution containing 65 % of water and 35 % of DMSO. It seemed like water-DMSO trimers were formed at this particular concentration and this sensitivity was the manifestation of changes in the local structure of the solvent, i.e., the formation or dissolution of $H_2O$ clusters. The authors concluded that together with its enhanced water solubility, the cyanated lumazine derivate could be used for non-destructive DMSO detection in vitro for applications [16].

In this work, our aim is to develop an in vivo DSMO sensing technique utilizing solvatochromic response of fluorescence dyes. Among the various solvatochromic dyes, Indocyanine green (ICG) is

the most widely used NIR dye for fluorescence imaging [17–23]. Its absorption peak lies around 800 nm where biological tissue attenuates the fluorescence less and generates low autofluorescence [8]. Furthermore, hemoglobin absorption stays low and has an isosbestic point at 800 nm. Despite these spectroscopic merits of ICG in the 800 nm spectral window, the use of ICG has been limited to visualize blood perfusion volume and tissue permeability rate-based physiological assessment due to the lack of molecular specificity.

To be able to measure this complex solvatochromic response of ICG, a fluorescence lifetime imaging technique has been introduced [24]. However, this fluorescence lifetime technique requires either pulsed laser or radio-frequency amplitude modulated light source. In addition, expensive high-speed electronics are necessary to measure the time-domain or the frequency-domain signals. Meanwhile, we have previously developed a novel hyperspectral excitation-resolved near-infrared fluorescence imaging system (HER-NIRF) based on a continuous-wave wavelength-swept laser [25]. Based on a semiconductor optical amplifier and a wavelength-selector consisting of a holographic transmission grating, a reflection mirror, and a galvo-scanner mirror, this laser source can provide any wavelength between 784 and 805 nm, a range that is particularly optimum for ICG absorption peak. In this study, this technique is applied for measuring the distribution of the therapeutic agent dimethyl sulfoxide (DMSO) by utilizing solvatochromic shift in the spectral profile of ICG. Since ICG is an U.S. Food and Drug Administration approved fluorescent dye, the technique presented in this paper has a great potential to guide DMSO applications *in vivo*.

## 2. Materials and Methods

### 2.1. HER-NIRF System

The use of near-infrared wavelength-swept lasers for biomedical imaging has been documented previously [26,27]. We previously developed a new type of wavelength-swept laser, whose output was optimized around 800 nm to excite ICG around its maximum absorption wavelength [28]. It has a holographic transmission grating and a Galvo-scanner utilized as a wavelength-selector to overcome the thermal instability induced by the traditional piezoelectric transducer-based wavelength-selectors, as shown in Figure 1a. A traveling-wave semiconductor optical amplifier (SOA) is used to give optical gain in working spectral range between 784 nm and 805 nm. A 10-dB fiber-optic directional coupler is attached to the SOA's output port and its 90% arm is utilized for the laser output. The other one, 10% arm, is linked to the external fiber-optic laser cavity to feedback stimulated light towards the traveling-wave SOA. A holographic transmission grating, a reflection mirror, and a Galvo-scanner mirror comprise the wavelength-selector. The output spectrum is measured by an optical spectrum analyzer. The selected spectra of the laser output are displayed in dBm, Figure 1b. The measured −3 dB swept bandwidth of the swept laser is 35 nm (785–820 nm) and the −10 dB swept bandwidth s 40 nm (780–820 nm) The averaged laser output power per sweep is measured as 4 mW.
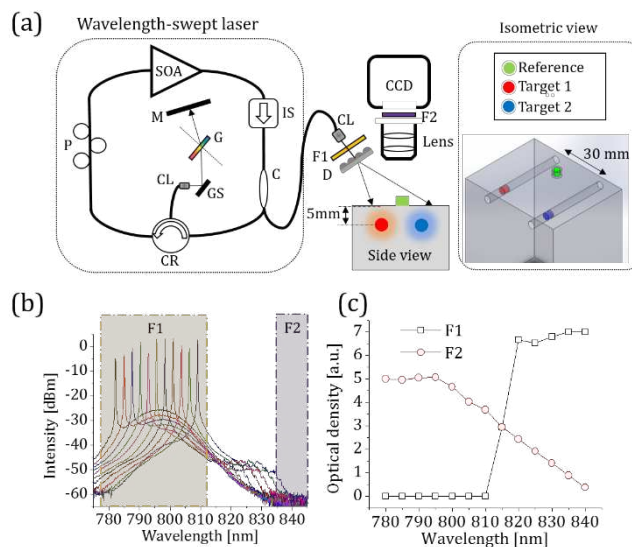
**Figure 1.** (a) A schematic diagram of the wavelength-swept laser and our HER-NIRF system. SOA: semiconductor optical amplifier, P: polarization controller, CR: circulator, CL: collimator, GS: Galvo-scanner, G: grating, M: mirror, C: coupler, IS: isolator, F1: exciter bandpass filter, D: diffuser, F2: emitter bandpass filter, CCD: charge coupled camera. (b) Measured output spectra of our wavelength-swept laser at different wavelengths. (c) A graph of the optical density of F1 and F2 over the wavelength range of interest.

The swept-wavelength laser is the core of the HER-NIRF system. After that a laser-line bandpass filter with a central wavelength of 794 nm, a bandwidth of 32 nm, and an out of band optical density (OD) of 7 is employed to clean up non-lasing components. The next component of the HER-NIRF system is an optical diffuser, which homogenizes the Gaussian laser beam with a power of less than 0.5 mW/cm². On the detection side of the HER-NIRF system, a CCD camera (ColdBlue, PerkinElmer optoelectronics, USA) with an imaging lens (Marco F/2.8, Sigma Inc., USA) is used to capture snapshots of fluorescence signals. The working distance of the imaging lens is 60 cm.

To test the HER-NIRF system, an agar phantom mimicking tissue optical properties is used (L 70 mm × W 50 mm × D 100 mm). In the field of biomedical optics, optical phantoms are frequently employed to mimic the optical characteristics of biological tissues [29]. They are created with optical characteristics that are similar to those of living human and animal tissues, such as light scattering and absorption coefficients. Agarose gels can be used to create homogeneous or heterogeneous structures, and their mechanical and physical properties are long-lasting. The turbidity and optical absorption of high-purity agarose gels are relatively low. As a result, the optical properties of agarose-based phantoms might be simply constructed with suitable light scattering and absorption agents [30]. Indian ink is used to adjust its absorption, while Intralipid is added to alter scattering properties. The absorption and reduced scattering coefficients of the phantom is adjusted to 0.0132 mm$^{-1}$ and 1 mm$^{-1}$, respectively. Two holes are prepared 5mm below the surface of the phantom be able to insert 3.2 mm (ID) ultra-thin wall glass tubes that are used as inclusions. The tubes are filled with different BSA-ICG and DMSO-ICG solutions.

An emitter bandpass filter that has a central wavelength of 840 nm, a bandwidth of 10 nm, and an average OD of 5 is used to collect the fluorescence emission. Figure 1c shows the measured OD of the filters used in this HER-NIRF system in the absence of ICG. As the wavelength of our swept laser approaches the fluorescence collection band, the performance of our system is degraded by the excitation light leakage. This reduces the signal-to-noise ratio and yields to incorrect fluorescence measurements [13].

Figure 1c shows the measured OD of the filters used in this HER-NIRF system in the absence of ICG. As the wavelength of our swept laser approaches the fluorescence collection band, the performance of our system is degraded by the excitation light leakage. This reduces the signal-to-noise ratio and yields to incorrect fluorescence measurements [13]. Therefore, HER-NIRF images

need to be corrected by subtracting the excitation-leakage images collected in the absence of ICG. In order to measure the solvatochromic response of ICG, a ratiometric approach is employed to estimate a relative excitation shift in relation to a reference standard that can be either a well-known fluorescent dye or a priori fluoresce image data. By using the first-order approximation to the basic equation of fluorescence can be written as

$$F(\lambda) \approx I\eta \frac{\Omega}{4\pi} 2.303\varepsilon(\lambda)lc. \qquad (1)$$

where, $F$ (a.u.) is the steady-state fluorescence intensity, $I$ (a.u.) is the incident light excitation intensity on the target, $\Omega$ (sr) is the solid angle, $\varepsilon$ (mol$^{-1}\cdot$cm$^{-1}$) is the molar extinction coefficient as a function of the excitation wavelength $\lambda$ (nm) , $\eta$ (%) is the quantum yield, $l$ (cm) is the pathlength of excitation light through the fluorescence sample, and c is the concentration of the fluorescent dye

### 2.2. ICG characteristic in water, DMSO, and bounded to bovine serum albumin

Typically, ICG is dissolved into an aqueous solution before the ICG administration, which has its absorption peak at 780 nm. After the administration, ICG quickly and mostly binds to hydrophobic pockets of albumin and its absorption peak shifts to 805 nm [9]. We measured the absorption spectra of ICG in different conditions using a commercial spectrometer (USB2000, Ocean Optics Inc., USA) in our lab. Figure 2a shows the normalized absorption spectra of ICG in water, DMSO, and bounded to bovine serum albumin (BSA-ICG). Figure 1b demonstrates a complex behavior of ICG in mixtures of water, DMSO, and BSA, which mimics ICG in biological media such as lymph or blood in the presence of DMSO. First, ICG is mixed with bovine serum albumin (BSA, Sigma Aldrich, USA) with a concentration of 50 mg/ml to mimic the concentration of albumin in human plasma dissolved in distilled water [10]. This mixture is called BSA-ICG. After adding DMSO into the BSA-ICG in distilled water, one can observe that the varying amount of DMSO results in the absorption peak shift of ICG. At the volume fraction zero, the solution contains BSA, ICG and water. The absorption peak of this solution demonstrating that most of ICG is bound to BSA.
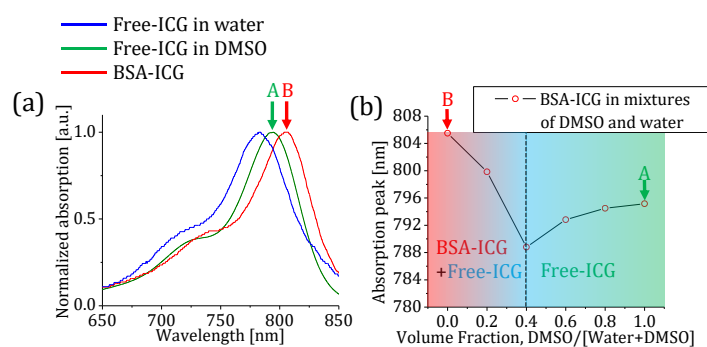


**Figure 2.** (a) The absorption spectra of ICG in different environments. The absorption peaks of BSA-ICG, ICG in DMSO and ICG in water are 805 nm, 795 nm, and 780 nm, respectively. (b)A graph that shows the absorption peak shift of a 6 μM BSA-ICG solution when added to different fractions of DMSO & water solutions. The BSA-ICG bond gradually breaks until the volume fraction of 0.4 and after that point all of ICG becomes free the BSA-ICG bond.

Our measurements shows that the BSA-ICG bond gradually breaks until the volume fraction of 0.4, the solutions in this volume fraction range contain BSA-ICG, free-ICG, BSA, water, and DMSO. One can observe that the absorption peak shifts to the shorter wavelength since free-ICG starts attributing to this absorption blue-shift. Between the volume fraction of 0.4 and 1, all of ICG becomes free from the BSA-ICG bond and its absorption spectrum solely depends on the polarity of the mixtures of solvents.

## 3. Results

### 3.1. The ratio of extinction coefficients of DMSO- and BSA-ICG

The change of the molecular environment affects the wavelength-dependent molecular extinction coefficient of ICG, and the spectral scan driven by our HER-NIRF system reveals the solvatochromic shift. One can assume a simplified case where the change of ICG concentration is trivial between the time sets of before and after the administration of DMSO. The ratiometric fluorescence of ICG in DMSO with respect to BSA-ICG in a dilute solution can be written as

$$\ln\left[F_D(\lambda)/F_B(\lambda)\right] = \ln\left[\varepsilon_D(\lambda)/\varepsilon_B(\lambda)\right] + \ln\left[\eta_D/\eta_B\right]. \tag{2}$$

where, the subscripts $B$ and $D$ describe BSA-ICG and ICG in DMSO, respectively. The right-hand side of Eq. (2) consists of a wavelength-dependent ratio of the extinction coefficients and a ratio of the quantum yields.

In order to confirm Eq. (2), we utilized the wavelength-swept laser to measure absorption of DMSO- and BSA-ICG at selected wavelengths in its operational range. The ratio of extinction coefficients of these two ICG solutions is shown in Figure 3a. Previous optical spectrometer absorption spectra measurements performed on the same DMSO- and BSA-ICG solutions are used as the control, Fig 2. Between 785 nm and 810 nm, the natural logarithmic ratio of extinction coefficients shows the maximum contrast and almost a linear decrease as a function of wavelength. In addition, the isosbestic point of DMSO- and BSA-ICG is found in the spectral range. Hence, we can model the ratio of extinction coefficients as a linear function of the excitation wavelength,

$$\ln\left[\varepsilon_D(\lambda)/\varepsilon_B(\lambda)\right] \approx m_{solvato}(\lambda - \lambda_{iso}). \tag{3}$$

where, $m_{solvato}$ (nm$^{-1}$) is the slope of our linear approximation and $\lambda_{iso}$ (nm) is the isosbestic wavelength of DMSO- and BSA-ICG in water solutions. In the maximum contrast window, the ratio of extinction coefficients in the different volume fractions are presented in Figure 3b. Calculated values of $m_{solvato}$ the various volume fractions are plotted as a function of the volume fraction in Figure 3c. One can compare Figure 2b with Figure 3c to find good correlation between our commercial spectrometer absorption measurements and the slope values of our linear model in Eq. (3) as shown in Figure 3d. Note that a 1 nm increase of the absorption peak of ICG corresponds to 1.45×10$^{-3}$ nm$^{-1}$ of the slope change in our ratiometric model.
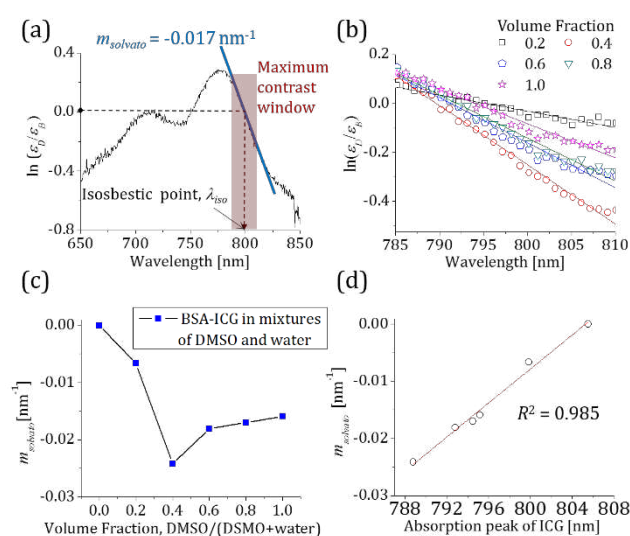


**Figure 3.** (a) The natural logarithmic ratio of the extinction coefficients of DMSO-ICG and BSA-ICG. A blue solid line shows a linear fit to the natural logarithmic ratio obtained with wavelength-swept laser between 785 nm and 810 nm [red-boxed area]. (b) A graph shows the slope change of a 6 μM BSA-ICG solutions when different amounts of DMSO added to change the volume fraction. (c) the

slope values of our linear model for different volume fractions of DSMO. (d) the change in the slope values w.r.t ICG absorption pear is nearly perfectly linear.

### 3.2. Phantom Experiment Results

To conduct tissue-like turbid medium experiments, an intralipid gelatin phantom is used ($\mu_a$= 0.0132 mm$^{-1}$, $\mu_s'$ = 1 mm$^{-1}$ at 800 nm). Two 3.2 mm long tubes, with a 3.2 mm inner diameter, filled with 26 μl of BSA-ICG and DMSO-ICG solutions are used for the experiments. A third identical BSA-ICG tube is used as the reference. In the first set of experiments all tubes are placed on top of the phantom for free-space measurements to eliminate the effect of scattering. Following that the BSA-ICG and DMSO-ICG tubes were placed deep inside the phantom, while the reference BSA-ICG tube is still kept on the surface. This arrangement allows to identify the effect of scattering on the CCD fluorescent measurements at different wavelengths. Despite the shift in the spectrum due to scattering, our method can separate BSA- and DMSO-ICG successfully based on the solvatochromic shift in the ICG fluorescence data.

### 3.2.1. Free-space measurements using CCD

Prior to phantom experiments, the ratiometri**c** fluorescence analysis is performed in free space using the CCD camera and the very same tubes. These measurements are unaltered and free of the spectral shift in the fluorescence signal due to migration of photons in a wavelength-dependent high scattering environment. Hence, these measurements can be used to confirm the previous measurements in Section 3.1, but using the HER-NIRF imaging set-up.

For this purpose, both BSA-ICG and DMSO-ICG tubes are placed on the top surface of the phantom together with the reference BSA-ICG tube, directly under the CCD camera. Fluorescence images at 50 different excitation wavelengths are acquired with a wavelength step of 0.5 nm. The mean fluorescence signals are extracted from regions of interest and used for computation of the ratiometric fluorescence and hence, the verification of Eq. (2). By incorporating Eq. (3) into Eq. (2), we obtain

$$\ln\left[\varepsilon_D\left(\lambda\right)/\varepsilon_B\left(\lambda\right)\right]+\ln\left[\eta_D/\eta_B\right]=m_{solvato}\left(\lambda-\lambda_{iso}\right)+b_{quantum}. \tag{4}$$

where, $b_{quantum}$ is the wavelength independent value of the relative quantum yield ratio. As seen from the black dots and line in Figure 4c, $b_{quantum}$ can be read at the isosbestic point and is 0.80, which means $\eta_D$ is 2.23 times higher than $\eta_B$. The calculated $m_{solvato}$ obtained from the relative fluorescence measurement in Figure 4c is -0.017 nm$^{-1}$, which shows good agreement with the calculated $m_{solvato}$ from our absorption measurements without imaging set-up, as shown in Figure 3a. As expected, the slope value between two identical fluorescence signals of the BSA-ICG tube and the reference BSA-ICG tube yields approximately zero as shown by the black dots and line in Figure 4b.
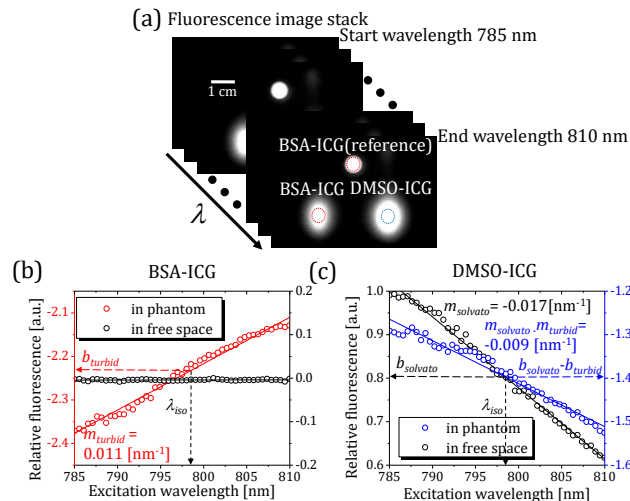
**Figure 4.** (a) The fluorescence image stack consists of 50 images obtained at different excitation wavelengths. Red-dashed circles indicate the reference BSA-ICG on the surface and the BSA-ICG embedded, in the phantom. A blue-dashed circle shows the DMSO-ICG region of interest. (b) The ratiometric measurements of BSA-ICG in free space and phantom with respect to the reference BSA-ICG. (c) The ratiometric measurements of DMSO-ICG in free space and phantom with respect to the reference BSA-ICG.

### 3.2.2. Phantom Measurements using HER-NIRF system

The turbid phantom experiment is designed to demonstrate the DMSO-ICG sensing performance of our HER-NIRF technique with the spectral distortion by multiple scattering. While the reference BSA-ICG tube is kept on top of the phantom, the second BSA-ICG tube is placed in the turbid phantom at a 5 mm depth as an experimental control, Figure 1a. The other tube filled with DMSO-ICG is also placed in the phantom at the same depth of the embedded BSA-ICG tube but 30 mm apart. Again, fluorescence images at 50 different excitation wavelengths are acquired with a wavelength step of 0.5 nm. The CCD camera integration time is 1 second per image.

Since the tubes are placed deep inside the turbid media, the spot size detected at the top surface of the phantom are much larger due to scattering, Figure 4a. The mean fluorescence signals are measured at the selected regions of interest indicated by the dashed-line circles in Figure 4a. The ratiometric fluorescence for BSA- and DMSO-ICG tubes with respect to the BSA-ICG reference is plotted as a function of the excitation wavelength as red and blue dots and lines in Figure 4b and 4(c), respectively. The ratiometric fluorescence between the reference BSA-ICG on surface and the BSA-ICG embedded in the phantom demonstrates a red-shift due to the multiple scattering which yields to a positive slope value in our ratiometric model, as shown in Figure 4b. Likewise, the multiple scattering shifts the measured relative excitation spectrum of DMSO-ICG by changing the slope value from -0.017 nm$^{-1}$ (in free space) to -0.009 nm$^{-1}$ (in phantom).

### 3.2.3. HER-NIRF spectral map for DSMO sensing

A fluorescence signal from an embedded ICG tube in a turbid medium can be written as

$$A(F) = F \exp\left[-\mu_{eff}(\lambda)2d\right]. \tag{5}$$

where, $A$ is the attenuation operator describing the Beer's law, $\mu_{eff}$ is the wavelength-dependent effective attenuation coefficient (mm$^{-1}$) and $d$ (mm) is the depth of the tube. The factor two describes the photon round trip. If both the reference and the embedded targets contain the same BSA-ICG, we obtain

$$\ln\left[\frac{A(F_B)}{F_B}\right] = -\mu_{eff}(\lambda)2d = m_{turbid}(\lambda - \lambda_{iso}) + b_{turbid}. \tag{6}$$

where, $m_{turbid}$ is the slope of the linear fit in Figure 4b that is equal to 0.011 nm$^{-1}$. The parameter $b_{turbid}$ is -2.23 which describes the wavelength-independent attenuation in the region of interest. If the embedded tube contains a different solution (DMSO-ICG) than the reference (BSA-ICG), we can use Eq. (2-6) to obtain

$$\ln\left[\frac{A(F_D)}{F_B}\right] = (m_{solvato} - m_{turbid})(\lambda - \lambda_{iso}) + (b_{quantum} - b_{turbid}). \tag{7}$$

In Figure 4c, $m_{solvato}$ corresponds to the slope of the black dots and line, while $(m_{solvato} - m_{turbid})$ corresponds to the slope the blue dots and line. The spectral distortion by multiple scattering affects the spectral content of DMSO-ICG measurements similarly to the result shown in Fig 4(b).

Based on this theory and our experimental results, we further applied our ratiometric technique to produce a pixel-by-pixel spectroscopic map. First, the fluorescence signal at each pixel is used as a numerator in the left-hand side of Eq. (7), while the fluorescence signal of the reference BSA-ICG on the surface is used as the denominator. Afterwards, the slope of the linear fit per pixel is attributed to the pixel under study to produce a spectroscopic image as shown in Figure 5a. When the pixels show approximately a zero slope, they identify fluorescence signals from the reference BSA-ICG on the surface. However, when the pixels show a positive slope, they belong to the multiple scattered fluorescence signals from the embedded BSA-ICG tubes.
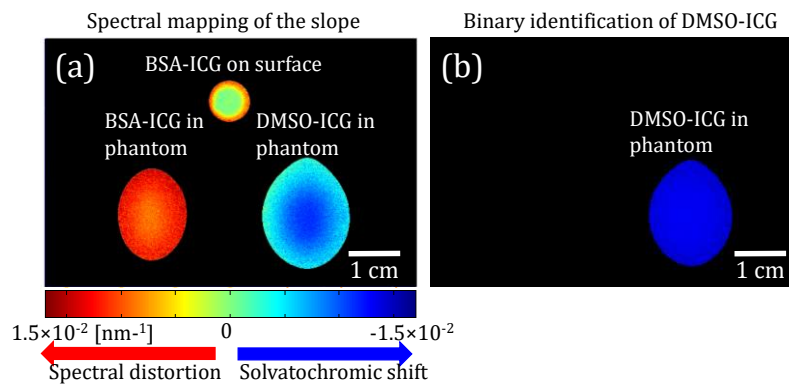


**Figure 5.** (a) A color-coded slope map shows the excitation blue-shift of the DMSO-ICG tube while the embedded BSA-ICG sample demonstrated a red-shift of excitation spectrum by multiple scattering. Low signal pixels from the intercept map are excluded from the image processing. (b) A binary identification map exclusively displays DMSO-ICG. All the pixels with slope values that are lower than a slope threshold are removed from the original spectral map.

Note that a positive slope is observed even around the container wall of the reference BSA-ICG due to scattering within the contained wall. A slope threshold of our linear fitting (-2.95 x 10$^{-5}$ nm$^{-1}$) is applied on the spectral map to generate a binary identification map of DMSO-ICG. Despite this spectral content degradation induced by multiple scattering, one can still identify the pixels of DMSO-ICG tubes in Figure 5b. These successful results shows that HER-NIRF system is a great tool for mapping DSMO distribution in thick turbid-media.

## 4. Discussion

In this work, we successfully demonstrate the potential of our proof-of-concept HER-NIRF system in monitoring DMSO distribution in turbid media. The spectroscopic measurement of the local polarity expands the information contents of conventional wide-field fluorescence imaging

techniques. Our method is based on the solvatochromic shift of ICG, which depends on the local environment. DMSO amount in the local area regulates the amount of the solvatochromic shift and HER-NIRF system measures the extent of this shift to determine the DSMO amount in return. This methodology works perfectly in free space; however, the effect of scattering on the measured signals should be considered in turbid medium such as biological tissue. For this purpose, free-space measurements are performed first prior to using tissue simulating agar phantom, which is designed to mimic in vivo conditions. Different ICG solutions are embedded deep in the phantom to demonstrate the effect of the scattering on the measured fluorescence spectrum. Since the scattering in tissue is dominated by mie-scattering, it is wavelength dependent [31]. Hence, the lower wavelengths experience higher scattering that creates a red-shift in the fluorescence signals travelling from the ICG target to the surface.

Since the HER-NIRF system differentiates the DSMO solution by the solvatochromic shift that resembles blue-shift, scattering distorts the spectral information in the opposite way. Regardless, our measurements demonstrate that our HER-NIRF system can differentiate DSMO-ICG solution. Although the sign of the slope is used to qualitatively identify the presence of DMSO in each pixel, our measurements show that quantitative imaging can be possible if one can choose appropriate reference signals to minimize the spectral distortion. However, a reference point at the same depth may not be available for all applications. In such cases, one alternative strategy might be performing HER-NIRF imaging before and after the application of DMSO. Hence, determination can be made by considering the change in the slope of the ratiometric fluorescence of the same target. For example, if ICG is accumulated in lymph nodes and imaging is performed before and after the application of DMSO, the technique presented here can be applied since the depth of the reference and target will be the same.

The wavelength-swept laser is the key for our HER-NIRF technique due to its superior performance compared to other available light sources [16]. Being low-cost, fast in the spectral scan, and able to perform coherent light amplification, this wavelength-swept laser can be a very powerful light source for real-time measurement in various DSMO sensing/mapping applications. While its superior spectral resolution is a big advantage for this application, the HER-NIRF technique also provides much higher signal to noise ratio by measuring the whole fluorescence emission spectrum as opposed to conventional systems utilizing multiple or variable band-pass filters at the detection site. This will be important, particularly for the tomographic HER-NIRF application, where speed is important [25,32–34]. For in vivo applications that requires higher power, optical amplifiers can be utilized to amplify the signal output of the swept-wavelength source. Future tomographic applications will also allow 3D imaging as opposed to 2D mapping of DMSO demonstrated in this study.

One of the strengths of our technique is that the wavelength-swept laser at the core of our system works in the NIR range, centered around 800nm, where auto-fluorescence from the tissue components diminish. Hence, our technique is immune to the contamination of the auto-fluorescence signals originated from various tissue components. On the other hand, there are some weaknesses our system that should be noted. As seen from Figure 1c, the emitter bandpass filter F2 has a significantly larger bandwidth than the its originally stated bandwidth of 10 nm. This was due to the fact that the performance of the fluorescence emission filters unfortunately depends on the incident angle of the incoming photons. The performance of these filters is optimum when the photons hit the filter perpendicularly. However, in our camera-based system, they are positioned between the lens and the CCD camera, which makes their performance far from ideal. While the lens is focusing the image on to the CCD, different portions of the light beam pass through the filter with various angles that deteriorates the performance of the filter. Although there might be some ways to collimate the beam while passing through emission filter, in practical imaging applications this is the regular configuration so we chose to test the system under this imperfect conditions [17,35–37].

Meanwhile, it important to evaluate the detection limits of this technique. The error in the measured slopes, $m_{solvato}$ and $m_{turbid}$, is around 11% (0.0018 nm$^{-1}$). This error is nearly five times smaller than the change in the slope due the blue-shift due solvatochromic shift in DSMO, despite the

opposite red-shift in the fluorescence signals travelling from the ICG target to the surface, $m_{solvato}$–$m_{turbid}$ (0.0090 nm$^{-1}$). Therefore, the method of applying a thresholding worked as shown in our study. It should be noted that though, the red-shift due to the scattering depends on the depth of the inclusions, and the scattering of the medium. Therefore, the signal generated by the deeper inclusions will experience higher red-shift and at some point, when the error in the measured slopes is comparable to the $m_{solvato}$ - $m_{turbid}$, our technique will reach to its detection limit. Since there are two parameters that govern this limit, the reduced scattering coefficient of the medium and depth of the inclusion, the depth limit of our technique will depend on the tissue type. However, it might be safe to state that in regular tissues, our technique will be limited to 1cm.

The ability to measure distribution of DMSO in vivo can lead to a better understanding of the optimum DSMO concentration required for many therapeutic and drug delivery applications. Furthermore, such a system can guide those applications real-time by optimizing the DSMO dose in the future. On the other hand, this technique can also help increasing the knowledge of the pharmacokinetic properties of ICG in tissue. For instance, K. Licha et al. have demonstrated that increasing hydrophilicity of cyanine dyes enhances the fluorescence image contrast of tumor by inhibiting the plasma protein binding of these dyes [14]. Thus, the properties of DMSO inhibiting the albumin binding of ICG can lead to better understanding of the pharmacokinetics of ICG for tumor imaging. Finally, by providing additional spectral information, HER-NIRF technique can be applied for measuring solvatochromic response of other fluorescence dyes and even be adapted for endoscopic applications due to efficient light guiding by fiber optics.

## 5. Conclusion

In this study, we demonstrate a steady-state spectroscopic wide-field imaging technique that has the ability to resolve the solvatochromic response of ICG. The pivotal part of our imaging technique is a continuous-wave near-infrared novel wavelength-swept laser, which can tune its output wavelength with high speed and superior spectral resolution. The solvatochromic response of ICG depends on the local DMSO concentration. Hence, this HER-NIRF system can map the DMSO concentration in biological tissues and will be crucial in determining the best DMSO dose for a specific application, from improving medication delivery effectiveness to minimizing adverse response. More importantly, during these therapeutic applications, this technology may also direct the DMSO dose in real time.

**Author Contributions:** Drs Cho and Nouizi built the system and undertook the experimental studies. They also contributed to the system design and analyze the data. Drs Kim mostly spent effort on the development of the wavelength-swept laser, while Dr. Gulsen focused on the conceptualization of the DSMO sensing using HER-NIRF and supervised the study.

## References

1.  M. Karim, R.S. Boikess, R.A. Schwartz, P.J. Cohen, Dimethyl sulfoxide (DMSO): a solvent that may solve selected cutaneous clinical challenges, Arch Dermatol Res 315(6) (2023) 1465-1472.
2.  B.N. Swanson, Medical use of dimethyl sulfoxide (DMSO), Rev Clin Basic Pharm 5(1-2) (1985) 1-33.
3.  M.M. Paul, Interval therapy with dimethyl sulfoxide, Ann N Y Acad Sci 141(1) (1967) 586-98.
4.  A. Kulah, M. Akar, L. Baykut, Dimethyl sulfoxide in the management of patient with brain swelling and increased intracranial pressure after severe closed head injury, Neurochirurgia (Stuttg) 33(6) (1990) 177-80.
5.  E.E. ROSENBAUM, R.J. HERSCHLER, S.W. JACOB, DIMETHYL SULFOXIDE IN MUSCULOSKELETAL DISORDERS, JAMA 192 (1965) 309-13.
6.  R. Peeker, M.A. Haghsheno, S. Holmäng, M. Fall, Intravesical bacillus Calmette-Guerin and dimethyl sulfoxide for treatment of classic and nonulcer interstitial cystitis: a prospective, randomized double-blind study, J Urol 164(6) (2000) 1912-5; discussion 1915-6.

7.  S. Amemori, R. Iwakiri, H. Endo, A. Ootani, S. Ogata, T. Noda, S. Tsunada, H. Sakata, H. Matsunaga, M. Mizuguchi, Y. Ikeda, K. Fujimoto, Oral dimethyl sulfoxide for systemic amyloid A amyloidosis complication in chronic inflammatory disease: a retrospective patient chart review, J Gastroenterol 41(5) (2006) 444-9.

8.  K. Marren, Dimethyl sulfoxide: an effective penetration enhancer for topical administration of NSAIDs, Phys Sportsmed 39(3) (2011) 75-82.

9.  A. Otterbach, A. Lamprecht, Enhanced Skin Permeation of Estradiol by Dimethyl Sulfoxide Containing Transdermal Patches, Pharmaceutics 13(3) (2021).

10. G. Liu, J. Li, S. Deng, Applications of Supercritical Anti-Solvent Process in Preparation of Solid Multicomponent Systems, Pharmaceutics 13(4) (2021).

11. G. Pauli, W.L. Tang, S.D. Li, Development and Characterization of the Solvent-Assisted Active Loading Technology (SALT) for Liposomal Loading of Poorly Water-Soluble Compounds, Pharmaceutics 11(9) (2019).

12. V.D.a.B.B.N.a.S.E.M.-M.a.T.M.N.a.S.S.a.P.O.a.V.M.a.J.L.a. Phiwayinkosi, Chapter 25 - The impact of dimethyl sulfoxide on oxidative stress and cytotoxicity in various experimental models, in: B.P.a.V.R.P. Vinood (Ed.), Toxicology, Academic Press2021, pp. 243-261.

13. C. Morris, L. de Wreede, M. Scholten, R. Brand, A. van Biezen, A. Sureda, E. Dickmeiss, M. Trneny, J. Apperley, P. Chiusolo, G.W. van Imhoff, S. Lenhoff, G. Martinelli, M. Hentrich, T. Pabst, F. Onida, M. Quinn, N. Kroger, T. de Witte, T. Ruutu, C.M.a.L.W.P.o. EBMT, Should the standard dimethyl sulfoxide concentration be reduced? Results of a European Group for Blood and Marrow Transplantation prospective noninterventional study on usage and side effects of dimethyl sulfoxide, Transfusion 54(10) (2014) 2514-22.

14. B. Kollerup Madsen, M. Hilscher, D. Zetner, J. Rosenberg, Adverse reactions of dimethyl sulfoxide in humans: a systematic review, F1000Res 7 (2018) 1746.

15. A. Marini, A. Muñoz-Losa, A. Biancardi, B. Mennucci, What is solvatochromism?, J Phys Chem B 114(51) (2010) 17128-35.

16. J. Truksa, M. Kratochvíl, J. Richtár, L. Ivanová, M. Weiter, J. Krajčovič, V. Lukeš, Spectroscopic behavior differences between lumazine and alloxazine in the DMSO-water mixture, Spectrochim Acta A Mol Biomol Spectrosc 302 (2023) 122998.

17. A.H. Chao, S.A. Schulz, S.P. Povoski, The application of indocyanine green (ICG) and near-infrared (NIR) fluorescence imaging for assessment of the lymphatic system in reconstructive lymphaticovenular anastomosis surgery, Expert Rev Med Devices 18(4) (2021) 367-374.

18. B.E. Schaafsma, F.P. Verbeek, D.D. Rietbergen, B. van der Hiel, J.R. van der Vorst, G.J. Liefers, J.V. Frangioni, C.J. van de Velde, F.W. van Leeuwen, A.L. Vahrmeijer, Clinical trial of combined radio- and fluorescence-guided sentinel lymph node biopsy in breast cancer, Br J Surg 100(8) (2013) 1037-44.

19. J.R. van der Vorst, M. Hutteman, J.S. Mieog, K.E. de Rooij, E.L. Kaijzel, C.W. Lowik, H. Putter, P.J. Kuppen, J.V. Frangioni, C.J. van de Velde, A.L. Vahrmeijer, Near-infrared fluorescence imaging of liver metastases in rats using indocyanine green, J Surg Res 174(2) (2012) 266-71.

20. B.E. Schaafsma, J.R. van der Vorst, K.N. Gaarenstroom, A.A. Peters, F.P. Verbeek, C.D. de Kroon, J.B. Trimbos, M.I. van Poelgeest, J.V. Frangioni, C.J. van de Velde, A.L. Vahrmeijer, Randomized comparison of near-infrared fluorescence lymphatic tracers for sentinel lymph node mapping of cervical cancer, Gynecol Oncol (2012).

21. P. Huang, X. Intes, S. Nioka, a.B. Chance, Simulation of delivery of ICG injected intravenously into human subject for breast cancer detection, SPIE 4929 (2003) 322-329.

22. M. Gurfinkel, A.B. Thompson, W. Ralston, T.L. Troy, A.L. Moore, T.A. Moore, J.D. Gust, D. Tatman, J.S. Reynolds, B. Muggenburg, K. Nikula, R. Pandey, R.H. Mayer, D.J. Hawrysz, E.M. Sevick-Muraca, Pharmacokinetics of ICG and HPPH-car for the detection of normal and tumor tissue using fluorescence, near-infrared reflectance imaging: a case study, Photochem Photobiol 72(1) (2000) 94-102.

23. S. Yoneya, T. Saito, Y. Komatsu, I. Koyama, K. Takahashi, J. Duvoll-Young, Binding properties of indocyanine green in human blood, Invest Ophthalmol Vis Sci 39(7) (1998) 1286-90.

24. M.Y. Berezin, H. Lee, W. Akers, S. Achilefu, Near infrared dyes as lifetime solvatochromic probes for micropolarity measurements of biological systems, Biophys J 93(8) (2007) 2892-9.

25. G. Farouk Nouizi and Jaedu Cho and Maha Algarawi and Chang-Seok Kim and Gultekin, Application of a wavelength-swept laser for spectrally resolved wide-field near-infrared fluorescence imaging, Opt. Continuum 1(8) (2022) 1768--1776.

26. H.L.a.J.F.d.B.a.B.H.P.a.E.C.W.L.a.R.Y.a.S.H. Yun, Optical frequency domain imaging with a rapidly swept laser in the 815--870 nm range, Opt. Express 14(13) (2006) 5937--5944.

27. D.M.a.M.T.E.-H.a.I.B.a.L.A.T.a.L.M.a.N.G.a.A.M.R.a.C.B.a. Joseph, Simultaneous multimodal ophthalmic imaging using swept-source spectrally encoded scanning laser ophthalmoscopy and optical coherence tomography, Biomed. Opt. Express 8(1) (2017) 193--206.

28.  J. Cho, G. Gulsen, C.-S. Kim, 800-nm-centered swept laser for spectroscopic optical coherence tomography, Laser Physics 24(4) (2014) 045605.

29.  A. Mustari, I. Nishidate, M.A. Wares, T. Maeda, S. Kawauchi, S. Sato, M. Sato, Y. Aizu, Agarose-based Tissue Mimicking Optical Phantoms for Diffuse Reflectance Spectroscopy, J Vis Exp (138) (2018).

30.  M. Lualdi, A. Colombo, B. Farina, S. Tomatis, R. Marchesini, A phantom with tissue-like optical properties in the visible and near infrared for use in photomedicine, Lasers Surg Med 28(3) (2001) 237-43.

31.  D.A. Boas, M.A. O'Leary, B. Chance, A.G. Yodh, Scattering and wavelength transduction of diffuse photon density waves, Physical Review. E. Statistical Physics, Plasmas, Fluids, and Related Interdisciplinary Topics 47(5) (1993) R2999-R3002.

32.  F. Nouizi, J. Brooks, D.M. Zuro, S.K. Hui, G. Gulsen, Development of a theranostic preclinical fluorescence molecular tomography/cone beam CT-guided irradiator platform, Biomed Opt Express 13(11) (2022) 6100-6112.

33.  F. Nouizi, T.C. Kwong, J. Ruiz, J. Cho, Y.W. Chan, K. Ikemura, H. Erkol, U. Sampathkumaran, G. Gulsen, A thermo-sensitive fluorescent agent based method for excitation light leakage rejection for fluorescence molecular tomography, Phys Med Biol 64(3) (2019) 035007.

34.  H. Jang, G. Lim, K.S. Hong, J. Cho, G. Gulsen, C.S. Kim, Effect of Shot Noise on Simultaneous Sensing in Frequency Division Multiplexed Diffuse Optical Tomographic Imaging Process, Sensors (Basel) 17(12) (2017).

35.  A.B. Thompson, E.M. Sevick-Muraca, Near-infrared fluorescence contrast-enhanced imaging with intensified charge-coupled device homodyne detection: measurement precision and accuracy, J Biomed Opt 8(1) (2003) 111-20.

36.  S. Yu, T. Yao, B. Yuan, An ICCD camera-based time-domain ultrasound-switchable fluorescence imaging system, Sci Rep 9(1) (2019) 10552.

37.  B. Zhu, E.M. Sevick-Muraca, A review of performance of near-infrared fluorescence imaging devices used in clinical studies, Br J Radiol 88(1045) (2015) 20140547.